Matter and Radiation at Extremes

RESEARCH ARTICLE

pubs.aip.org/aip/mre

Ion emission from warm dense matter produced by irradiation with a soft x-ray free-electron laser

Cite as: Matter Radiat. Extremes 9, 016602 (2024); doi: 10.1063/5.0157781
Submitted: 11 May 2023 • Accepted: 4 September 2023 •
Published Online: 14 November 2023

Josef Krása,[1,a)] Tomáš Burian,[1] Věra Hájková,[1] Jaromír Chalupský,[1] Šimon Jelínek,[1,2,3] Kateřina Frantálová,[1] Michal Krupka,[1,2,4] Zuzana Kuglerová,[1] Sushil Kumar Singh,[1,2] Vojtěch Vozda,[1] Luděk Vyšín,[1] Michal Šmíd,[5] Pablo Perez-Martin,[5] Marion Kühlman,[6] Juan Pintor,[7] Jakub Cikhardt,[8] Matthias Dreimann,[9] Dennis Eckermann,[9] Felix Rosenthal,[9] Sam M. Vinko,[10,11] Alessandro Forte,[10] Thomas Gawne,[10] Thomas Campbell,[10] Shenyuan Ren,[10] YuanFeng Shi,[10] Trevor Hutchinson,[12] Oliver Humphries,[13] Thomas Preston,[13] Mikako Makita,[13] Motoaki Nakatsutsumi,[13] Xiayun Pan,[5,14] Alexander Köhler,[5] Marion Harmand,[7] Sven Toleikis,[6] Katerina Falk,[1,5,14] and Libor Juha[1]

AFFILIATIONS

[1]Department of Radiation and Chemical Physics, Institute of Physics, Czech Academy of Sciences, Na Slovance 2, 182 21 Prague 8, Czech Republic
[2]Laser Plasma Department, Institute of Plasma Physics, Czech Academy of Sciences, Za Slovankou 3, 182 00 Prague 8, Czech Republic
[3]Department of Surface and Plasma Science, Faculty of Mathematics and Physics, Charles University in Prague, V Holešovičkách 2, 180 00 Prague 8, Czech Republic
[4]Department of Physical Electronics, Faculty of Nuclear Science and Engineering Physics, Czech Technical University in Prague, V Holešovičkách 2, 180 00 Prague 8, Czech Republic
[5]Helmholtz-Zentrum Dresden-Rossendorf, Bautzner Landstraße 400, 01328 Dresden, Germany
[6]DESY Photon Science, Notkestraße 85, D-22607 Hamburg, Germany
[7]Institut de Minéralogie, de Physique des Matériaux et de Cosmochimie, UMR 7590 – UPMC/CNRS/IRD/MNHN, Sorbonne Université, 4 place Jussieu, 75005 Paris, France
[8]Department of Physics, Faculty of Electrical Engineering, Czech Technical University in Prague, Technická 2, 166 27 Prague 6, Czech Republic
[9]Center for Soft Nanoscience, University of Münster, Busso-Peus-Straße 10, D-48149 Münster, Germany
[10]Department of Physics, Clarendon Laboratory, University of Oxford, Parks Road, Oxford OX1 3PU, United Kingdom
[11]Central Laser Facility, STFC Rutherford Appleton Laboratory, Didcot OX11 0QX, United Kingdom
[12]Lawrence Livermore National Laboratory, 7000 East Avenue, Livermore, California 94550, USA
[13]European XFEL GmbH, Holzkoppel 4, D-22869 Schenefeld, Germany
[14]Technische Universität Dresden, 01062 Dresden, Germany

[a)]**Author to whom correspondence should be addressed:** krasa@fzu.cz

ABSTRACT

We report on an experiment performed at the FLASH2 free-electron laser (FEL) aimed at producing warm dense matter via soft x-ray isochoric heating. In the experiment, we focus on study of the ions emitted during the soft x-ray ablation process using time-of-flight electron multipliers and a shifted Maxwell–Boltzmann velocity distribution model. We find that most emitted ions are thermal, but that some impurities chemisorbed on the target surface, such as protons, are accelerated by the electrostatic field created in the plasma by escaped electrons. The morphology of the complex crater structure indicates the presence of several ion groups with varying temperatures. We find that the ion

sound velocity is controlled by the ion temperature and show how the ion yield depends on the FEL radiation attenuation length in different materials.

 https://doi.org/10.1063/5.0157781

I. INTRODUCTION

Experiments devoted to laser–matter interaction have provided characteristics of various mechanisms of generation and acceleration of ions, which have not only stimulated ideas for many applications, but also contributed to the understanding of laser–matter interactions. Despite the small number of free-electron laser (FEL) x-ray facilities around the world, they are very attractive areas of research such as the science of warm dense matter (WDM) and high energy density,[1–3] multiphoton ionization,[4] coherent diffraction imaging,[5] femtosecond x-ray holography,[6] and cluster physics.[7] Although many diagnostic techniques have been introduced for the probing of WDM, as presented by Falk,[8] comprehensive research on ion emission seems to remain in the background.

The ablation of thick targets by femtosecond laser pulses and the associated ablation rates have been elucidated using models considering the thermal dependences of the optical and thermal parameters of the irradiated materials.[9–11] It is evident that ultrashort laser pulses can create a very high temperature within a very small volume of both metal and polymer targets. In some experiments, it is important to show that they provide negligible heat diffusion into the material. In such cases, the profile of the crater created on the surface of the target can be used to characterize focused soft x-ray laser beams.[12,13]

On the other hand, when plasma is produced by the interaction of a femtosecond x-ray laser with a target, the obtained dependence of ion emission on the focus position can determine the optimal focus position, which has a strong dependence on peak intensity.[14–16] In this case, the position of the focal plane refers to the position where the highest proton energy is measured. However, when the crater created does not have a single-hole shape with a smooth surface, as shown in Refs. 12 and 13, but a complex structure of discrete, clearly outlined circular holes and shallow lobes at the bottom of the ablated craters, as shown in Ref. 14, then the secondary craters can become secondary sources of ions expanding into the vacuum with different velocity distributions.

In this paper, we apply a simple model of a signal from time-of-flight (TOF) detectors, which is based on the shifted Maxwell–Boltzmann distributions, to quantify the parameters of ion currents emitted by plasma produced with the use of an FEL. Application of this model makes it possible to reveal partial currents of ionized species, j, which form the total current of ions detected with the use of an ion detector located outside the critical zone, where the charge states of ions of the expanding plasma are frozen.[17] This model allows us to determine the temperature T_i and center-of-mass kinetic energy $E_{\mathrm{CM}\text{-}i}$ of ions. The value of $E_{\mathrm{CM}\text{-}i}$ indicates whether the ion groups are accelerated by an electrostatic potential ($\phi_{ef} = E_{\mathrm{CM}\text{-}i}/e$) generated by the release of fast electrons from the plasma ($E_{\mathrm{CM}\text{-}i} > 0$) or whether they are only a part of thermal plasma ($E_{\mathrm{CM}\text{-}i} = 0$) freely expanding into vacuum.

The remainder of this paper is organized as follows. Section II describes the experimental station at the soft x-ray free-electron laser FLASH2 at DESY, Hamburg and the TOF detector that was used, as well as a method for determining the morphology of the crater surface. Section III presents an analysis of TOF signals and characteristics of ion emission, which are based on a three-dimensional model of the TOF signals detailed in the Appendix. To conclude, we discuss the correlation between the revealed currents of singly charged ions and the complex morphology of the crater surface.

II. EXPERIMENTAL ARRANGEMENT

Foil targets of Al, Cu, Fe, Ni, Si, GaAs, and poly(methyl methacrylate) (PMMA), ranging in thickness from 0.1 to 1 mm, were irradiated with the soft x-ray FEL FLASH2 using a Kirkpatrick–Baez focusing system with a focal length of 200 cm to focus 100-fs pulses with energies between 10 and 100 μJ and a wavelength of 13.5 nm (91.8 eV photon energy) to a 36 μm-sized spot surrounded by shallow lobes, resulting in intensities reaching 10^{13} W/cm^2 on targets.[18] Since the x-ray attenuation length $L_{\mathrm{att}} < 2$ μm for the targets used, the target thickness does not affect the laser–target interaction. The pulse energy was obtained from an in-line gas monitor detector (GMD), prior to arrival of the pulses at the interaction region.[19] The crater characteristics were obtained with the use of Nomarski-type microscopy. The angle of incidence of the laser beam on the target was 22.5°, as shown in Fig. 1. The fluctuation of the laser energy from pulse to pulse was below 10%. Exposures were done at various focal positions (FP) relative to the target surface to determine the focus position FP = 0, which corresponds to a coincidence of the minimum focus with the front target surface. The convention used is as follows: FP < 0 means the focus position is in front of the target surface and FP > 0 means it falls inside or behind the target. The FP was moved in the range from −20 to 20 mm. The samples were

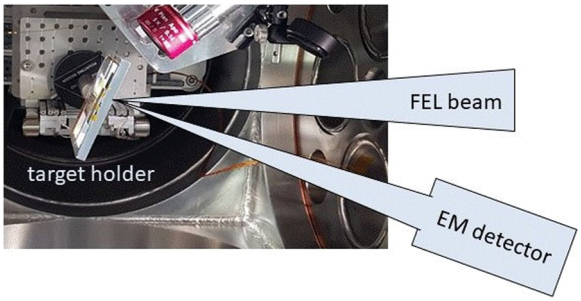

FIG. 1. Experimental setup of the ion experiment at FLASH2. The FEL beam hits the target from the right at a 22.5° angle. Ions are detected along the target normal with an open electron multiplier located 24 cm from the target.

further inspected by Nomarski optical microscopy and white-light interferometry.

The produced ions were detected with the use of an open electron multiplier (EM) type 119EM along the target surface normal at 24 cm from the target. This windowless electron multiplier equipped with Be–Cu dynodes was manufactured by Thorn EMI Electron Tubes, UK. It has a Venetian blind structure, with a ten-slat entrance dynode with radiation aperture of 2.16 cm diameter and a total of 17 dynodes. The initial amplification of electron current certified by the manufacturer was 6.26×10^6 with an operating voltage of −3 kV applied to the first dynode, while the input grid was grounded. The cross-section of a measured ion beam overlapped the input (radiative) aperture of the 119EM. Calibration of electron multipliers is needed for ion detection, because the ion-induced emission of electrons from the first dynode depends not only on the quality of the dynode's surface but also on the intercepted ion species and their potential and kinetic energies.[20] The calibration has shown that the EM gain depends mainly on the charge state of detected ions, with a weaker dependence on the impact velocity. Since the we were unable to calibrate the gain of the open EM during this experiment, we used previous data[21] for the range of low ion kinetic energies encountered in our experiment to determine the value of this gain as 5×10^5.

For the analysis of the EM signal, it is necessary to find out how this signal depends on the velocity, energy, and number of ions incident on the first EM dynode. This dependence is characterized by a parameter α, the value of which affects the shape of the TOF signal according to the three-dimensional model of an ion detector signal recalled in the Appendix:

$$S(L,t,\alpha)dS\,dt \propto v_x^{\alpha} f(\vec{v})d\vec{v}, \tag{1}$$

where $f(\vec{v})$ is the three-dimensional velocity distribution function, $v_x = L/t$ is the ion velocity in the detector direction, L is the distance of the ion detector from the target, and

$$\alpha = \begin{cases} 0 & \text{if the response is proportional to the number (density) of incident particles,} \\ 1 & \text{if the response is proportional to the stream (current) of incident particles,} \\ 2 & \text{if the response is proportional to the energy deposited by particles.} \end{cases}$$

Thus, it is necessary to know the dependence of the current gain (amplification factor) $G_c = j_{EM}/j_i$ on the velocity of detected ions. In our experiment, multicharged ions before impact on the first dynode were accelerated by an applied EM bias of −3 kV, which increased their impact velocity. Figure 2 shows the EM signal induced by Ni^{q+} ions and three calculated dependences for q = 1–3 of their impact velocities enlarged by this bias. This calculation shows that the impact velocity of ions on the first dynode of the detector is almost time-independent for TOF > 3 μs, i.e., the detector signal is almost independent of the velocity and energy of ions at the input grounded grid of the detector, and therefore α = 0. However, the energy of ions whose TOF is ~0.5 to 3 μs is comparable to the energy they additionally acquire when accelerated by the bias of −3 kV. Thus, the detector signal is affected by the velocity of the incoming ions, and α = 1. Whether the value of α is equal to 0 or 1 can also be verified by finding the best fit of Eq. (1) to the EM signal for these values.

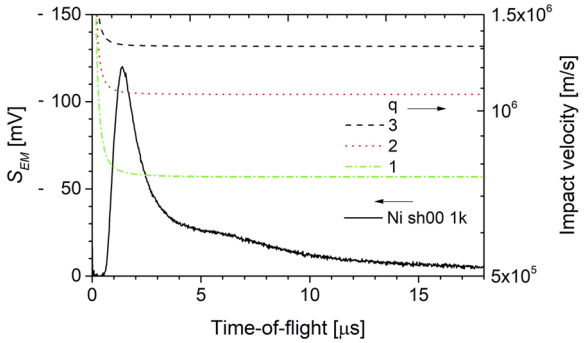

FIG. 2. Signal of the 119EM electron multiplier induced by ions produced by interaction of FEL beam with Ni target (solid line) and TOF dependence of impact velocity of Ni^{q+} ions on the first dynode affected by an EM bias of −3 kV, which was calculated for charge states q of 1–3 (dashed lines).

The fluence profile of the 13.5 eV FEL beam focused on the target and the corresponding spot size were determined using the fluence scan (F-scan) method and the nonlinear response function recovery (NoReFry) algorithm.[22,23] Both methods use laser-induced ablation in PMMA to determine the profile of the non-Gaussian energy distribution of the focused laser beam, which can significantly affect the experimental characteristics of ion emission. While the fluence scan method[12] exploits microscope images of PMMA ablative imprints created on the target surface by the focused laser beam, the NoReFry algorithm[23] works with two-dimensional depth profiles of ablated craters acquired using atomic force microscopy (AFM). The F-scan method recovers beam iso-fluence contours at various fractional levels with respect to the maximum, from which the fluence curve is derived. The NoReFry algorithm retrieves a general two-dimensional fluence profile. The effective areas A_{eff} of the foci as determined using the F-scan method and NoReFry algorithm are 1027 ± 123 μm^2 and 952 ± 247 μm^2, respectively. The calibration curve, which determines the dependence of the crater depth on the pulse energy of the 13.5 nm radiation, allowed us to determine the radiation attenuation length L_{att} = 178 ± 5 nm for the PMMA target that was used. The normalized fluence profile, obtained by converting the AFM-measured imprints on the PMMA target to

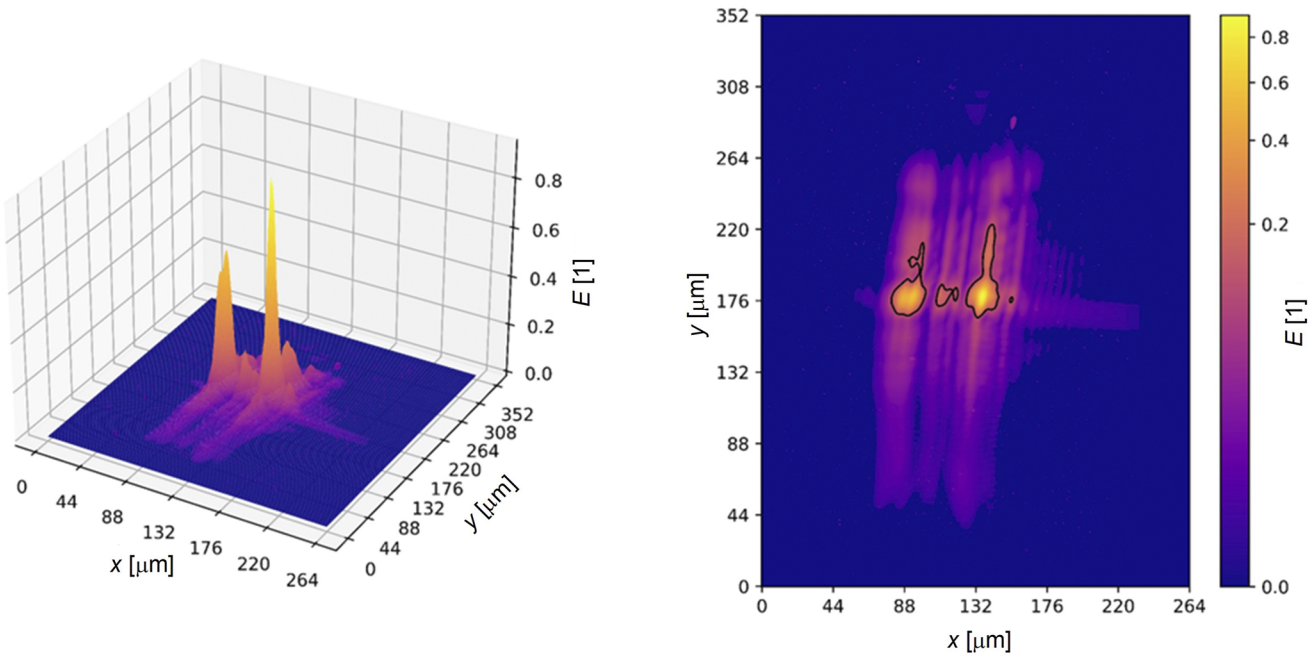

FIG. 3. Normalized fluence profile of the focused laser beam obtained by converting the measured imprints, i.e., the depth profile of the crater created on the surface of the PMMA target, to laser fluence. The black solid curve indicates an iso-fluence contour encircling an area equal to the effective area of 1027 μm^2, which corresponds to an effective beam radius of 36 μm.

laser fluence with the use of the calibration curve, is shown in Fig. 3. The reconstruction of the laser energy profile shows two intense peaks surrounded by wide, low-intensity lobes. The black solid curve drawn in the iso-smooth contour (see Fig. 3, right) encloses an area equal to an effective area of 1027 μm^2, corresponding to an effective beam radius of 36 μm.

III. EXPERIMENTAL RESULTS AND DISCUSSION

A. Ion sound velocity

The TOF spectra of ions produced by focusing the soft x-ray FLASH2 beam on thick Al, Fe, Ni, GaAs, PMMA, and Si foil targets had to be detected with the use of an electron multiplier because of their very small current at the nanoampere level. Figure 4 shows typical TOF spectra of ions emitted by irradiated targets. These spectra show similar behavior in each material, since they have two dominant maxima corresponding to fast and slow ions. Thus, we can assume that the TOF spectrum consists of a series of individual, overlapping currents of various ionized species. The fastest ions, which form the front of the expanding plasma plume, are hydrogen ions produced from chemisorbed impurities, such as hydrocarbons, on the target surface.[14,15] These protons should be accompanied by carbon and eventually oxygen ions that again have been produced from impurities. In addition to these ionized impurities, the TOF spectrum may also contain currents of slowly propagating charged clusters of the heavier target atoms.[14]

Separation of the laser-produced plasma into fast and slow groups is a common phenomenon observed in other experiments performed in various laboratories using both FEL and standard femtosecond lasers.[14,24–27] Another way to demonstrate the separation of fast and slow ions is to transform the ion detector signal into the spatial distribution of the ion charge density Q_i at a selected time τ that has elapsed since the laser–target interaction. This is made

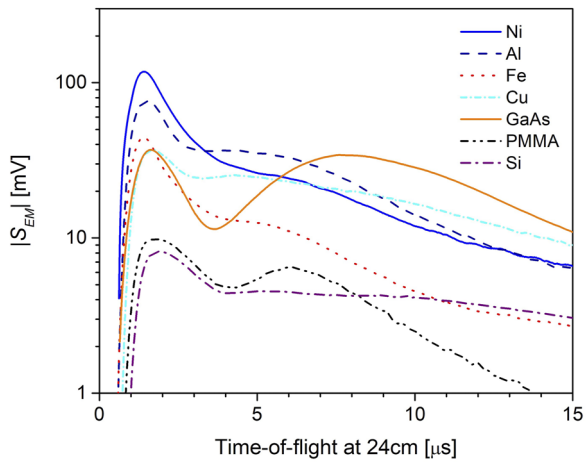

FIG. 4. Signals from the 119EM electron multiplier induced by ions produced by interaction of the soft x-ray FLASH2 beam with Al, Fe, GaAs, Ni, PMMA, and Si targets. The TOF spectra were measured at 24 cm from the targets. The intensity on the targets was 2.8×10^{13} W/cm^2 and FP = 0.

possible by a method based on transformation of the TOF signal acquired by the detector into a DOF (distance-of-flight) dependence of the ion charge density $Q_i(z, \tau)$. This method was derived and experimentally verified for ions that have passed a critical distance beyond which recombination of ions is negligible; in this case, the charges are non-interacting and thus the ion charges are "frozen". The similarity relation for the ion current density measured at different distances from the target is $j(z, \tau)z^3 = j(L, t)L^3$, where $z/\tau = L/t = v$, which follows from the assumption of conservation of the charge carried by ions far from the target, whose density decreases as L^{-2}. This can be also derived from Eq. (1) by modifying the term L/t^4 to v^4/L^3 in $d\vec{v} = \left(L/t^4\right)dS\,dt$, where dS is the area element of the ion detector, as provided in the Appendix. As a result, the detector signal decreases with distance as L^{-3}. The TOF t is transformed to the DOF z using the relationship $z = L\tau/t$, where L is the detector distance from the target. The values of τ and L are kept fixed. On substituting t by z, the ion current density $j(L, t) = Q(L, t)\ v$ can be transformed to the space-resolved ion charge density at τ as[28]

$$Q_i(z, \tau) = j(z)\tau L^3/z^4. \tag{2}$$

Since the relationship (2) corresponds exactly to the three-dimensional ion expansion, which results in the ion rarefaction observed at longer distances from the target, as mentioned above, the actual changes in the density gradient in the near zone, where the recombination occurs, are greater than the changes determined by the method used in Ref. 17.

DOF spectra are presented in Fig. 5 for $\tau = 1\ \mu$s. These spectra also show how far from the target the ion front has spread within 1 μs. Since the ion expansion is closely related to the electron distribution, the ion density should decrease exponentially with distance.

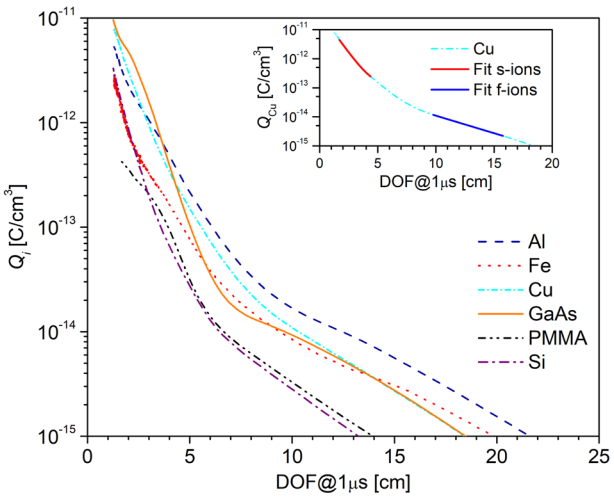

FIG. 5. DOF spectra obtained by transformation of signals from the 119EM electron multiplier induced by ions produced by interaction of the soft x-ray FLASH2 beam with Al, Fe, GaAs, Ni, PMMA, and Si targets for a time of 1 μs that has elapsed since the laser–target interaction. The intensity on the targets was 2.8×10^{13} W/cm^2. The inset shows two fits of Eq. (3) to the DOF spectrum of Cu ions to estimate the ion sound velocity associated with slow (red line) and fast (blue line) ions.

This can be expressed in the form $n_i(z, t) = n_0 \exp(-v/c_s)$, where $n_i(z, t)$ is the density of those ions traveling at velocity v, n_0 is the density at the emitting surface, and c_s is the ion sound velocity.[29] Substituting $v = z/\tau$ gives

$$n_i(z, \tau) = n_0 \exp\left(-\frac{z}{\tau c_s}\right), \tag{3}$$

where τ is the above-mentioned chosen time and $c_s = (kT_{ef}/m_i)^{1/2}$ is the ion sound velocity. kT_{ef} is generally a function of the charge state q of ions, their temperature T_i, and the electron temperature T_e. If T_{ef} does not change during the ion expansion, this curve follows a single-exponential decrease over the whole range. Assuming that the mean charge state of ions is $\bar{q}$, and e is the elementary charge, then the expansion function $n_i(z, t) = Q_i(z, t)/e\bar{q}$ can be fitted to the DOF spectrum. However, Fig. 5 shows that the rate of decay varies with distance, and thus only short sections of the DOF spectrum can be considered as a simple exponential decay, manifesting as linear on a semi-logarithmic scale. It can be assumed that in this short section, the values of $\bar{q}$ and T_{ef} change only slightly. Then, the fitted value of $\tau\ c_s$ allows us to calculate the corresponding values of kT_{ef}.

A fit of the exponentially decreasing function $a_0 \exp(-z/\tau c_s)$ to the DOF spectrum of Cu ions shown in the inset of Fig. 5 gives kT_{ef} values of ≈40 and ≈840 eV. These values can be interpreted as the kT_{ef} corresponding to slow and fast ions.[30] In summary, the analysis of the DOF spectra of all studied elements using Eq. (3) shows that kT_{ef} of fast ions reaches hundreds of eV (i.e., 200–1000 eV), while for slow ions it is tens of eV (10–90 eV).

The two-temperature model still does not fit the data exactly, and therefore we use a multitemperature model with partial currents. Ions are not only separated into two basic groups of fast and slow ions, but into several groups with different expansion velocities. In addition to temperature, the expansion velocity of ions is also affected by the center-of-mass velocity that the ions acquire by accelerating in an electrostatic field created by escaping fast electrons, as will be discussed below. This fact should also be reflected in the parameters of partial currents revealed by decomposition of TOF spectra. A break in the exponential decrease in density with increasing distance from the target should also occur at the front of the plasma, which contains fast hydrogen ions, i.e., the lightest species. However, owing to the high velocity of H^+ ions, this break should occur at DOF ≈ 20–50 cm for $\tau = 1\ \mu$s, where their density is quite negligible. The decline in the rate of decrease of charge density, located at a distance of 5–10 cm from the target, corresponds to the minima of the TOF spectra, occurring at 3–5 μs after the pulse (see Fig. 4). In this location, no hydrogen impurities can occur, and hence the rate drop can be interpreted as a significant change in temperature of Cu ions.

B. Ion velocity distribution

Since the use of an ion mass analyzer was not possible in this experiment, the number of partial ion currents could only be estimated by fitting the TOF spectra with a composite function S consisting of variable number of currents. For revealing these partial currents, we used a signal function recalled in the Appendix, which is based on the shifted Maxwell–Boltzmann distribution:

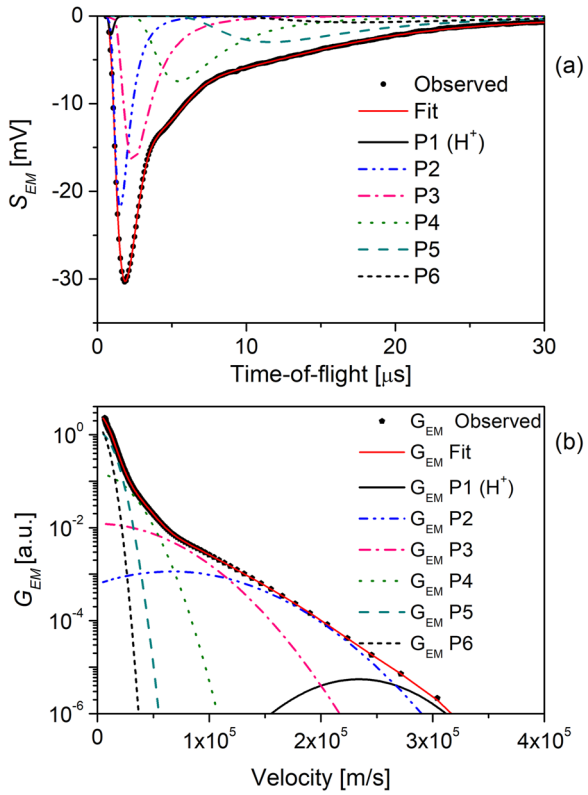

FIG. 6. (a) Fitting of TOF spectrum of ions to partial currents P1–P6. (b) Gaussian parts G_{EM} of P1–P6 currents of the TOF signal function in (a). P1 and P2 peaks of beam-like ions ($u_{CM\text{-}P1} \approx 2.3 \times 10^5$ and $u_{CM\text{-}P2} \approx 6.7 \times 10^4$ m/s) and P3, . . ., P6 peaks of thermal ions emitted by Ni target irradiated with 1.4×10^{13} W/cm^2.

$$S = \frac{L}{t^4}\sum_{i,q} S_{i,q}\,\exp\left[-\frac{m_i}{2kT_{i,q}}\left(\frac{L}{t} - u_{CM-i,q}\right)^2\right], \tag{4}$$

where i denotes the ionized species with mass m_i and charge state q, which form a partial current density $j_{i,q}$ with amplitude $S_{i,q}$, $u_{CM\text{-}i,q}$ is their center-of-mass velocity directed to the ion collector, k is the Boltzmann constant, and $T_{i,q}$ is the temperature. An example of fitting of (4) to an EM signal induced by Ni ions is shown in Fig. 6(a). Since the ion population is equilibrated at the time of observation and ion charge states are "frozen", the relationship (4) can be used to describe the ion momentum distribution. Obviously, fitting the shifted Maxwell–Boltzmann distribution to the TOF spectrum is a phenomenological choice that allows us to make a simple quantitative comparison between different shots.

Figure 6(b) shows the Gaussian part of the decomposed detector signal defined as

$$G_{EM} = \left|\frac{t^4}{L}S(L,t)\right|, \tag{5}$$

which represents the sum of Gaussian distributions corresponding to currents of groups of ions in Eq. (4). If the $u_{CM:i,q}$ value of an i,q-group is nonzero, then the maximum of the corresponding Gaussian function is shifted from zero. These ion groups can be considered as beam-like ions.

Along with the ionized target species, ionized surface impurities are also emitted from the irradiated target surface.[14,15] A typical contaminant is hydrogen, whose ions emitted from the periphery of the crater can expand at a velocity comparable to that of the slower ions forming the group of fast ions, and therefore can cause signal smearing. However, their contribution to signal smearing depends on their amount, which tends to be negligible compared with the amount of ionized target species. Thus, although a very small number of slow H^+ ions can be detected using a mass analyzer, the fitting (4) to the detector signal may not identify them because, for example, the second derivative of the detector signal that should indicate them does not show a clear change.[31]

Fitting of Eq. (4) to the ion current emitted from the irradiated Ni target reveals six groups of ions. Consistent with other experiments, the fastest group, labelled P1, can be considered as a group of fast H^+ ions.[14,31] These ions are accelerated to the highest velocity and move at the front of the expanding plasma. The following peaks should correspond to multiply charged ions of the irradiated target elements. In a plasma with several ion species, each with a different value of q/m_i, the ambipolar electric field that appears in the collisional regime tends to accelerate these different species relative to each other.[32] This leads to their observable separation during expansion, where their charge gradually decreases with decreasing expansion velocity.[33,34]

Figure 6(b) shows two ion groups P1 and P2, which consist of beam-like ions accelerated by escaped electrons, because their Gaussian distribution has a maximum at velocities of 2.3×10^5 m/s for hydrogen ions and 6.7×10^5 m/s for Ni ions. The potential corresponding to the acceleration of H^+ ions was about 300 V. This indicates that in the plasma front layer there are fast electrons escaping from the plasma and a potential barrier accelerating the ions. This process is influenced by collisions of electrons before their escape, the ratio of the height of the potential barrier to the temperature of fast electrons, oscillations of the potential barrier, etc. This potential partially shielded by H^+ ions also accelerated the P2 group of Ni^{q+} ions to a center-of-mass energy of 1.3 keV. This allows us to estimate the charge state of these ions to be 5. The charge state of the slower groups should gradually decrease to 1, as mentioned above. Conversely, the other four ion groups have Gaussian distributions G_{EM}P3, . . ., G_{EM}P6 centered around zero because their $u_{CM} \approx 0$. Therefore, they can be considered as thermal ions. The kT parameters of the P1 and P2 currents reached values of about 20 eV and 2.2 keV, respectively, while the slower thermal ions forming the P3–P6 groups reached lower values of about 1.5 keV, 300, 65, and 30 eV, respectively.

Numerical simulations of the plasma produced on bulk samples, for example, of niobium and vanadium, by the FLASH laser have shown that the plasma reaches temperatures between 100 and 400 eV at a power density above 10^{16} W/cm^2.[14] Although the intensity in our experiment was three orders of magnitude lower, the observed temperature of the fastest ion groups was comparable or higher, as shown in Fig. 7, where the temperature is related to the relative atomic mass A_r. [The term m_i/kT in Eq. (4) is substituted by $m_u/(kT/A_r)$, where m_u is the atomic mass constant.] The temperature of the fastest ion group (labelled as P1) can be interpreted as the temperature of H^+ ions in all TOF spectra.

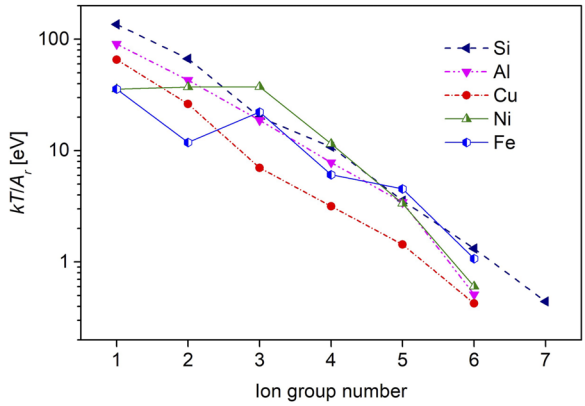

FIG. 7. Temperature per relative atomic mass kT/A_r for irradiated targets vs order of ion groups (partial peaks). Numbering of the revealed ion groups starts from the fastest one.

The best fits showed that all ion currents except the Si ion current consisted of six partial currents, while for Si ions seven partial currents were revealed. The seventh group represents the slowest ions forming the long tail of the TOF spectrum, which is not found in other plasmas, as shown in Fig. 4. Some experiments have shown that there are groups of the slowest singly charged ions forming very long tails of TOF spectra, which can be interpreted as the sum of two groups.[33] Therefore, both groups P6 and P7 could be formed only by Si^+ ions.

As shown in Fig. 7, kT/A_r values of Cu ions (P2–P6 peaks) decrease with the peak number almost exponentially from ~26 to 0.4. Comparison of the relevant values of $kT \approx 1600$ and 30 eV with the $kT_{ef} \approx 840$ and 40 eV evaluated using the ion sound model (3) indicates (i) T_{ef} represents the average temperature of corresponding ion groups, (ii) the contribution of T_e to the ion sound velocity c_s is negligible.

The temperature per relative atomic mass kT/A_r of the first two ion groups of the Si plasma shown in Fig. 7 reaches the highest values of all five irradiated target materials, even though their total current is the lowest. It is evident that the decrease in temperature of H^+ ions is influenced by the properties of the target, such as electrical conductivity, which affects the energy distribution of laser-excited electrons between chemisorbed and target atoms. Figure 7 helps to recognize the gradual temperature decrease from Si to Al and Cu targets, as the electrical conductivity of Al and Cu increases. However, Ni and Fe targets show the lowest temperature of H^+ ions, indicating that the H^+ ions have not been thermalized, because they gained center-of-mass energy. Conversely, all groups of Si, Al, and Cu ions have $u_{CM} \approx 0$ and are therefore thermal ions. The slower groups of Ni and Fe ions, i.e., groups 3, 4, etc., also have $u_{CM} \approx 0$. Compared with the properties of ions produced by IR–UV lasers, this is an exceptional case, because usually all ion groups have a nonzero u_{CM}.[34] This result could indicate that the value of the applied fluence is close to the threshold at which enough fast electrons are produced capable of contributing to the acceleration of Ni and Fe ions expanding into the vacuum, at the expense of their complete thermalization. It can be expected that a similar phenomenon would occur with other materials if the device used could provide more energy. It is interesting that of all the materials used, it is the Ni and Fe targets that emit the largest number of fast ions from the total number of produced ions. This could also be related to the morphology of the craters, which varies from one material to another in a strong dependence on the properties of the laser pulse, specifically on their periphery which is the source of slow ions. This fact would indicate that chemical bonds of impurities on the target surface, defects in the surface, and the amount of disorder usually present on surfaces also affect the energy distribution of excited electrons. Thus, the results need further theoretical and experimental investigation to be fully understood.

The formation of slower groups of ions may be related to a secondary process triggered by an imperfection of the laser beam, which can be determined from the crater morphology. In our case, there would have to be several secondary ion sources, possibly as many as seven, as can be inferred from the number of sub-craters shown in Fig. 8 for the Si and Cu targets. The observed crater morphology follows the power density distribution in the beam profile, which is affected by astigmatism and other aberrations of the laser beam originating predominantly from the beamline optics and the undulator source. The created sub-craters can emit ions because the resolidification of the surface layer takes about 100 ns.[35]

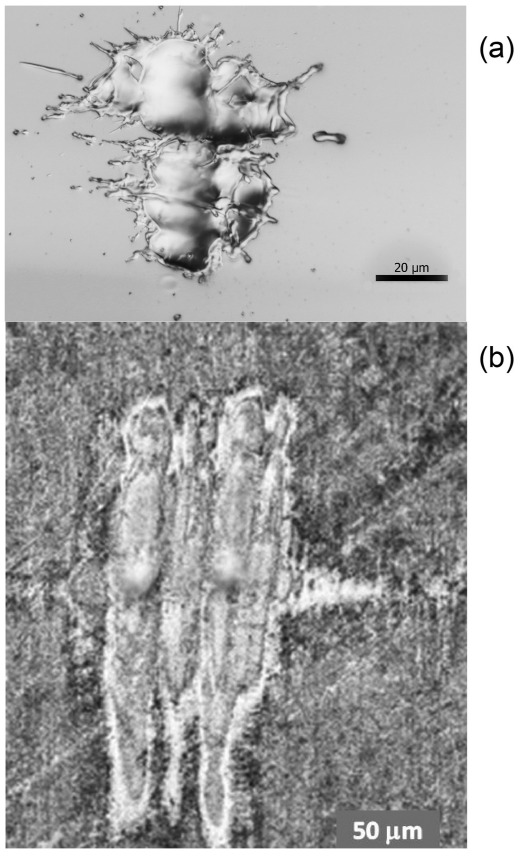

FIG. 8. Ablative imprints in (a) Si and (b) Cu created by 13.5-nm FLASH2 beam delivering energies of 100 and 50 μJ, respectively, on the targets.

In an ideal experiment, the crater formed around the circular focus acts as the sole source of ions. However, the high number of ion groups with $u_{CM} \approx 0$ indicates that the crater formed on the Si target, as Fig. 8(a) shows, can be understood as a complex of at least four sub-craters whose morphology corresponds to the power density distribution in the laser beam profile. This can provide an explanation for the observed multiple temperature phenomena. Figure 8(b) shows the threshold contour surrounding two circular craters localized at the intensity maxima of the laser beam (see Fig. 3) and an imprint of the peripheral surroundings of the central laser beam on the front surface of the Cu target. This beam imprint is larger than the imprint on the Si target, although the energy supplied was halved, i.e., 50 μJ, which indicates that the ablation threshold of Cu is lower than of Si at the wavelength of 13.5 nm.

The difference in the morphology of the craters on Si and Cu target surfaces may be due to different material properties, such as the attenuation length L_{att} of the FEL radiation in the surface layer, where the L_{att} in Cu is about 40 times shorter than that in Si,[36] as well as different material responses at applied FEL intensities,[37] the surface roughness height, etc. The absorption length is also related to the ablation threshold. More-penetrating radiation usually has a higher ablation threshold in terms of threshold fluence. Since the FEL (92 eV) is tuned close to the L-edge of silicon (99 eV), the radiation absorption is very low. In conclusion, the complex structure of discrete, clearly outlined circular/oval holes and shallow lobes at the bottom of ablated craters can act as a series of almost independent ion sources producing mostly thermal ions with various temperatures. Thus, the morphology of the crater surface can be interpreted as an assemblage of several separate sub-craters that reflect the fluence profile of the focused laser beam and that act as separate ion sources. This fact could be detected thanks to the imperfect profile of the laser beam.

In contrast to the presented single-element materials, the separation of GaAs plasma into fast and slow groups is the largest. However, owing to the mass proximity of Ga and As ions, there is no significant spatiotemporal separation between the expanding ^{31}Ga and ^{33}As ions, for both slow and fast ions. This proximity does not allow the currents of Ga and As ions to be distinguished from each other. The sum of their currents can be interpreted as a current of ions with an atomic mass equal to the average mass of the participating elements.

The fast bunch of GaAs plasma expands into vacuum at a peak velocity of 1.5×10^5 m/s, which is 4.75 times the expansion velocity of the slow plasma. The fast plasma manifests as a pair of partial peaks P1 and P2, where the peak P1 corresponds to beam-like H^+ ions because their $E_{CM} \approx 25$ eV and $kT \approx 80$ eV. The second peak P2 is composed only of thermal ions with $kT/A_r \approx 49$ eV and $E_{CM} \approx 0$. The slow thermal ions forming peaks P3–P5 have $kT/A_r < 3$ eV. This is the real reason for their separation during their expansion into the vacuum and the corresponding discontinuity in the exponential decrease in the DOF spectrum of the ion charge density. Since the Fig. 9 shows that the highest energy density supplied by the FEL onto the target surface was concentrated in two paraboloidal craters, we can assume that the fast plasma, i.e., the P1 and P2 peaks, originates from this pair of craters, while the slow plasma forming the P3–P5 groups of thermal ions comes from the shallow lobes. The deep minimum in the TOF spectrum [see Fig. 9(b)] between the groups of

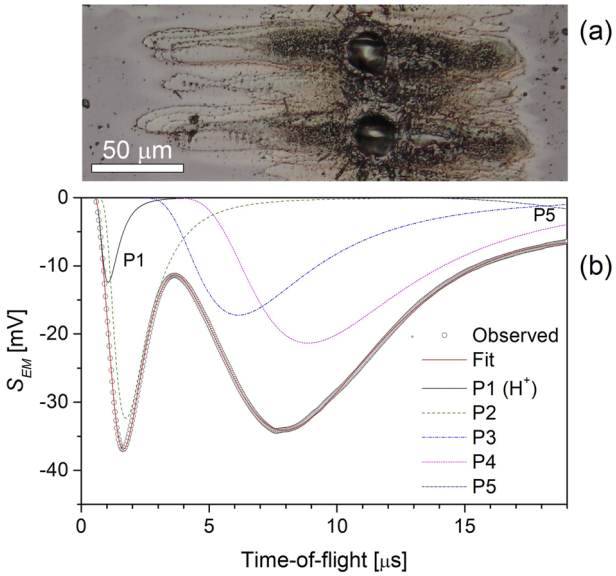

FIG. 9. (a) Ablative imprints in GaAs and (b) TOF spectrum of ions emitted by the GaAs target irradiated with energy 100 μJ (2.7×10^{13} W/cm^2).

peaks P1–P2 and P3–P5 proves that there is a difference between their acceleration mechanisms.

As an example, Fig. 10 shows the laser energy dependence of the peak energy E_{peak}/A_r of partial currents of expanding Ni plasma. The numbering of the partial current is related to the highest energy E_{peak}/A_r, where the fastest group of H^+ ions is labelled P1. The novelty of this experiment is that increasing the energy from 10 to 50 μJ creates a new fast ion peak, while the number of slow partial ion groups is preserved. This new peak (P2) could be interpreted as a group of Ni^{5+} ions, while the highest charge state of the Ni^{q+} ions produced at 10 μJ is 4 (here, the group of Ni^{4+} ions is also labelled P2). A further increase in laser energy only increases the magnitude

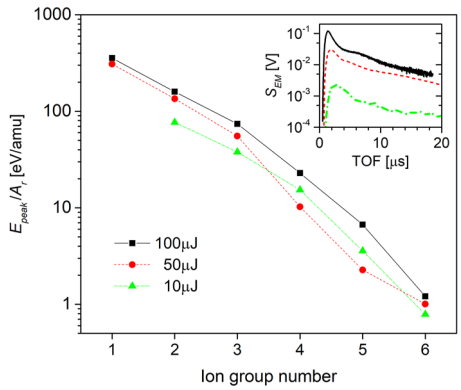

FIG. 10. Peak energy per relative atomic mass E_{peak}/A_r of partial ion groups revealed from TOF spectra. E_{peak} corresponds to the peak current of ions forming the nth group. The inset shows the corresponding TOF spectra of ions produced on a Ni target exposed to laser energies of 100, 50, and 10 μJ.

of the current and the temperature of the ions, while the number of ion groups does not change. Since the ion current and the ion expansion velocity increase with increasing laser energy, the dependence of the Ni ion emission on laser energy does not bring any unexpected changes.

C. Energy and charge carried by ions

To gain a more comprehensive understanding of the production of fast and slow ions, we will consider the energy E_{IC} of the ion collector signal as represented by the output voltage U_{IC} that is induced by the current of the captured ions:

$$E_{IC} = \int_0^{\infty} \frac{U_{IC}^2}{\mathrm{Re}(Z)}\, dt, \tag{6}$$

where the oscilloscope input impedance $Z = 50\ \Omega$. In this experiment, where an open electron multiplier is used, the corresponding ion current gain must be accounted for.

Applying this method, we can determine the amount of laser pulse energy that has been transferred by ions to the ion collector circuit, as shown in Fig. 11. Evident separation of fast ions from slow ions makes it easy to identify their gradual contribution to energy transfer. In the first period after laser interaction with a target, lasting 4 μs, only fast ions transfer energy into the electrical circuit of the ion detector. Then, the fast ions are replaced by slow ions, which transfer energy for another 15 μs. Figure 11 shows that from the laser energy of 100 μJ, only 7×10^{-22} J was transferred into the ion collector circuit. Thus, the efficiency of this energy transfer is only $\approx 7 \times 10^{-18}$. The contribution of slow ions to the energy transfer is $\approx$3.8 times higher than that of fast ions, as estimated from the partial ion currents revealed in Fig. 10. We note that the group of fast ions consists of partial currents of P1 and P2 groups, and the partial currents P3–P5 form the current of slow ions.

In general, H^+ ions followed by target ions having the highest kinetic energy and charge state form the front of the expanding plasma.[33,34] Since the ion mass analyzer could not be used in this experiment, the highest charge q state of the dominant ionized species can only be estimated. At lower intensities of the FLASH2 FEL, multiple charged ions were observed in Refs. 14–16. In our experiment, the highest value of q could reach 5, depending on the target element, as already experimentally demonstrated for the same photon energy in Ref. 16. Recombination of ions gradually reduces q as they become neutralized. In addition, ionized clusters and neutral particles can be produced. Because the electrostatic field accelerating the ions was very small in our experiment and affected mainly ionized hydrogen (see Figs. 5 and 6), there was no force to visibly separate the ions with different charges as observed in other experiments.[33,34] The presented decomposition of the TOF spectra using the Maxwell–Boltzmann distribution shows that the ions were separated according to their temperature. This separation of ions by temperature, but without the presence of a field, does not mean that the revealed partial currents are composed only of ions having the same charge and mass. In the case of PMMA, the current of slow ions coming from the shallow lobes of the craters exposed to low intensity can be composed of ionized fragments, for example, $C_2H_3^+$, COH^+ and/or $C_2H_5^+$, $C_3H_3^+$, $COCH^+$ and/or $C_3H_5^+$, $COCH_3^+$ and/or $C_3H_7^+$, $COOC^+$ and $COOCH^+$, as observed by photon-stimulated desorption of ions from a solid PMMA target irradiated with synchrotron radiation.[38]

A specific feature of our experiment is the very short attenuation length of the FLASH2 radiation in irradiated target materials, which ranges from tens to hundreds of nanometers. By irradiating the surface of different materials with the same laser intensity, we can obtain the dependence of the charge carried by ions (i.e., the time integral of the observed ion current) on the attenuation length L_{att}, as shown in Fig. 12 for optimal focusing (FP = 0). We note that the attenuation length was not corrected for the angle of incidence in this case. The values of the penetration depth indicate that the laser intensity is absorbed in the first atomic layers, leading to ablation and plasma production in the upper surface layer. The increasing L_{att} leads to a decrease in the deposited energy density heating the irradiated volume, which causes a decrease in the energy efficiency of the laser in ion production. The experiment apparently shows that less energy is stored in the sharp circular focus than outside because the fast ions carry less charge than the slow ions from the shallow lobes of the crater.

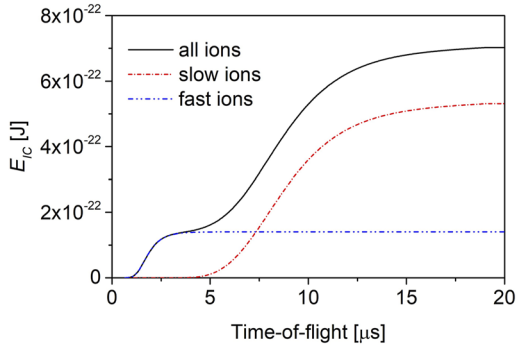

FIG. 11. Calculated time course of the energy E_{IC} transferred by current j_{IC} flowing through the input impedance of the oscilloscope. The solid line is for "all ions," for which $j_{IC} = S_{EM}/1.25 \times 10^{13}$ A, where S_{EM} is the EM signal (see Fig. 9). The other two lines show the hypothetical cases of generation of either fast or slow ions by a GaAs target irradiated with the 13.5-nm FLASH2 FEL.

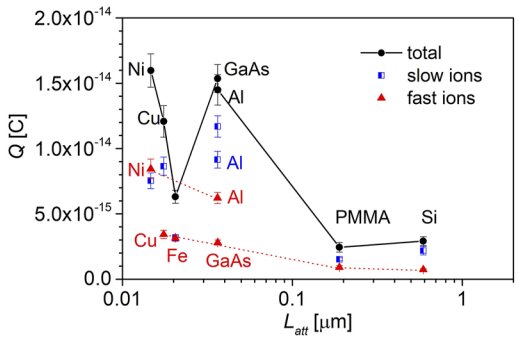

FIG. 12. Dependence of the charges Q_{fast} and Q_{slow} carried by fast and slow ions, respectively, and their sum on the attenuation length of 13.5 nm laser radiation in different targets. Attenuation lengths were calculated for all the target materials used using the Henke method.[36]

Determining the magnitude of the charges carried by the revealed currents shows that ion emission is affected by various interactions between laser-accelerated electrons with surface and lattice atoms. In the case of fast ions, the charge decreases with increasing penetration length of the 13.5 nm radiation. However, the charge of Ni and Al ions is about 2.5 times higher than that of the other fast ions. Higher charge yield is shown by slow ions. There are also two groups of material that differ in charge yield. The charge of slow ions emitted from Ni, Cu, Al, and GaAs materials is about four times greater than that from Fe, PMMA, and Si targets.

Since the laser intensity is more than ten times lower on the crater periphery than in the crater center (see the "effective area" in Fig. 3) and the charge yield is higher from the peripheral surroundings, the similarity in ion charge yields related to laser intensity or fluence is not relevant here. Thus, it can be assumed that the area of the crater periphery and post-interaction surface processes control the emission of slow ions whose temperature per relative atomic mass $kT/A_r \lesssim 10$ eV, as shown in Fig. 7, and the charge state of ionized fragments is low, mainly 1. The charges of Ni, Fe, PMMA, and Al fast ions are comparable to the charge of slow ions, while the charges of GaAs, Cu, and Si slow ions are about 3.5 times higher than that of fast ions. Other phenomena such as rapid surface pyrolysis of GaAs and other thermodynamic properties of GaAs[39] also contribute to the complexity of surface processes. It is evident that relaxation processes such as heat transfer from irradiated volume to target during the ablation period also play an important role.

The peculiarity of this experiment is that the ion emission originates from the surface layer, the submicrometer thickness of which depends on the attenuation length of the 13.5 nm FEL FLASH2 radiation in the irradiated targets. Although the results presented here require further theoretical and experimental investigation for their full understanding, it is possible to estimate the differences between the properties of plasmas produced using 100 fs FLASH and 23 ns KrF lasers at comparable fluences of 10–30 J/cm^2.[28,31,33] The fundamental difference between these experiments lies in the different mechanisms of energy dissipation in the irradiated targets. Whereas the nanosecond laser pulse interacts with the ablated material that remains in contact with the target, the femtosecond laser pulse does not interact with the ablated plasma, because the energy transfer time of the electron gas excited by the femtosecond laser to the lattice through collisions and the initiation of material ablation is about 10 ps. The interaction of the 23 ns KrF laser with the ablated plasma results in acceleration of ions, mainly by escaping electrons,[28,32] while the expansion of the ions produced by the FLASH2 laser is primary determined by the temperature of the ion component. Accordingly, the temperature of the ions produced by the soft x-ray laser is two orders of magnitude higher than that of the ions generated by the UV nanosecond laser. Conversely, nanosecond UV ablation of bulk targets produces ~10^7 times more ions than femtosecond soft x-ray ablation.

By contrast, a comparison of our extreme ultraviolet (XUV) experiment with an experiment devoted to the ablation of ionized silicon with 160 fs pulses delivered by a Ti:sapphire laser (800 nm, 600 μJ)[40] shows that the maximum kinetic energy of ions produced with the XUV laser is about 20 times higher. Numerous other authors[41–43] working with ultra-short pulses of UV–Vis–IR laser radiation obtained similar results as Roeterdink's group.[40,44] The basic characteristics of ions and electrons produced and accelerated by UV–Vis–IR lasers are scaled using the similarity parameter $I\lambda^2$ in W cm^{-2} μm^2.[45,46] To achieve a comparable value of maximum ion velocity, the Ti:sapphire laser experiment needs about 10 000 times higher $I\lambda^2$, mainly because of the very high value of the square of their wavelength ratio of ~3500. It is obvious that the properties of ions produced by these lasers cannot be compared using this similarity parameter, and therefore the model of interaction of UV–NIR lasers with matter is not applicable to XUV laser interaction experiments.

Changing the wavelength from 248–800 to 13.5 nm not only reduces the value of $I\lambda^2$ by a factor of ~300 to 3500, respectively, but also results in direct ionization by XUV photons whose energy is above the first ionization potentials of the target atoms. Each of these events also releases an energetic photoelectron. A portion of the photoelectrons can escape from the target into vacuum, carrying with them a cloud of secondary electrons, which are photoelectrons released from the basic atoms or ions of the solid target by collisional ionization. As result, a cloud of electrons is formed above the target surface, while there is a high excess of positive charge in the near-surface layer of the target, and the constitutional ions begin to be ejected from the material by Coulomb repulsion to be further accelerated after ejection by the electric field associated with the cloud of electrons previously released into the vacuum above the surface of the target. Other photoelectrons, however, transfer XUV energy to the target lattice by collisions with subsequent formation of multiply charged ions,[15] which contributes to material ablation. Our analysis also shows that the velocity of the fastest ions may contain a component that corresponds to the center-of-mass velocity caused by hot electrons escaping from the plasma, which were captured by the ions and formed a double layer with them.

Although little experimental data have been published to date, and it is therefore not possible to fully characterize XUV ion production, our analysis suggests that direct ionization of target atoms by high-energy XUV photons represents the primary process that distinguishes experiments with XUV lasers from those with UV–Vis–IR lasers.

IV. CONCLUSIONS

Ablation of solid films by ultrashort x-ray pulses delivered by the FLASH2 laser leads to the emission of multiple charged ions and ionized clusters. The proportion of both components can be influenced by changing the irradiation conditions and the target material. These conditions are affected by the aberrations of the laser beam and the attenuation length of the delivered 91.8 eV (13.5 nm) photons in targets, which determines the depth of the heated volume, where WDM can be transiently generated at ion temperatures of ≈1 eV.[47] Because the number of charged species produced in our experiments was very small, an open electron multiplier with a gain of 5×10^5 had to be used to detect them. We observed that the emission of ions by single-element materials is intense when the penetration depth of radiation is around 10 nm. The plasma expanding into vacuum consists of two ion parts: slow and fast ions, which vary greatly in temperature. The expansion of fast ions, including ionized hydrogen chemisorbed on the target surface, is influenced by the acceleration potential produced by fast electrons escaping from the plasma. Unlike fast ions, slow ions carry a substantial portion of

the charge generated by the laser pulse and transfer more energy to the ion collector circuit. We have estimated that the slow ions forming a substantial part of the plasma were emitted by the shallow lobes of the crater formed by the aberrations of the laser beam. Finally, a comparison of two different methods that allow determination of the ion sound velocity and the parameters of partial ion currents have allowed us to show that it is primarily the ion temperature that determines the ion sound velocity.

The transfer of laser energy by excited electrons to the submicrometer surface layer of the target depends not only on the target material, but also on the chemical bonds of contaminants on the target surface, defects in the surface, and the amount of disorder usually present on the surface. It is therefore difficult to draw undisputable conclusions from experiments in which the production of hot electrons and the transport of their energy to surface atoms varies from one target to another.

ACKNOWLEDGMENTS

This work is partly supported by EURATOM within the "Keep-in-Touch" activities and the Aquitaine Regional Council. We acknowledge financial support from the French National Research Agency (ANR) in the frame of the "Investments for the Future" Programme IdEx Bordeaux-LAPHIA (Grant No. ANR-10-IDEX-03-02), and the Czech Science Foundation (Grant Nos. GM23-05027M and 20-08452S). The team of K.F. are funded by the Helmholtz Association under Grant No. VH-NG-1338. A.F., T.G., T.C., S.R., Y.S., and S.M.V. acknowledge support from UK EPSRC Grant Nos. EP/P015794/1 and EP/W010097/1, and from the Royal Society. J.K., L.J., M.K., T.B., Š.J., and S.K.S. acknowledge support from the Czech Ministry of Education, Youth and Sports (Grant No. LM2023068).

AUTHOR DECLARATIONS

Conflict of Interest

The authors have no conflicts to disclose.

Author Contributions

Josef Krása: Conceptualization (equal); Writing – original draft (equal); Writing – review & editing (equal). **Tomáš Burian**: Conceptualization (equal); Investigation (equal); Methodology (equal); Resources (equal); Supervision (equal); Validation (equal). **Věra Hájková**: Data curation (equal); Formal analysis (equal); Investigation (equal). **Jaromír Chalupský**: Data curation (equal); Formal analysis (equal); Investigation (equal); Writing – review & editing (equal). **Šimon Jelínek**: Data curation (equal); Formal analysis (equal); Investigation (equal). **Kateřina Frantálová**: Data curation (equal); Investigation (equal). **Michal Krupka**: Data curation (equal); Formal analysis (equal); Investigation (equal). **Zuzana Kuglerová**: Data curation (equal); Formal analysis (equal); Investigation (equal). **Sushil Kumar Singh**: Data curation (equal); Investigation (equal). **Vojtěch Vozda**: Data curation (equal); Investigation (equal). **Luděk Vyšín**: Data curation (equal); Investigation (equal). **Michal Šmíd**: Data curation (equal); Investigation (equal); Writing – review & editing (equal). **Pablo Perez-Martin**: Data curation (equal); Investigation (equal). **Marion Kühlman**: Investigation (equal); Resources (equal). **Juan Pintor**: Data curation (equal); Investigation (equal). **Jakub Cikhardt**: Investigation (equal); Methodology (equal). **Matthias Dreimann**: Investigation (equal); Resources (equal). **Dennis Eckermann**: Investigation (equal); Resources (equal). **Felix Rosenthal**: Investigation (equal); Resources (equal). **Sam M. Vinko**: Conceptualization (equal); Data curation (equal); Investigation (equal). **Alessandro Forte**: Data curation (equal); Investigation (equal). **Thomas Gawne**: Data curation (equal); Investigation (equal). **Thomas Campbell**: Data curation (equal); Investigation (equal). **Shenyuan Ren**: Data curation (equal); Investigation (equal). **YuanFeng Shi**: Data curation (equal); Investigation (equal). **Trevor Hutchinson**: Data curation (equal); Investigation (equal). **Oliver Humphries**: Data curation (equal); Investigation (equal); Methodology (equal). **Thomas Preston**: Data curation (equal); Investigation (equal). **Mikako Makita**: Data curation (equal); Investigation (equal). **Motoaki Nakatsutsumi**: Data curation (equal); Investigation (equal). **Xiayun Pan**: Data curation (equal); Investigation (equal). **Alexander Köhler**: Data curation (equal); Investigation (equal). **Marion Harmand**: Conceptualization (equal); Investigation (equal); Methodology (equal); Project administration (equal). **Sven Toleikis**: Conceptualization (equal); Investigation (equal); Methodology (equal); Project administration (equal); Resources (equal). **Katerina Falk**: Conceptualization (equal); Funding acquisition (equal); Methodology (equal); Project administration (equal); Writing – review & editing (equal). **Libor Juha**: Conceptualization (equal); Funding acquisition (equal); Investigation (equal); Methodology (equal); Project administration (equal); Resources (equal); Writing – review & editing (equal).

DATA AVAILABILITY

The data that support the findings of this study are available from the corresponding author upon reasonable request.

APPENDIX: THREE-DIMENSIONAL MODEL OF TOF SIGNAL

The detection of ions has its particular features due to the mechanism of ion interaction with the detector, which also determines the minimum detectable signal level. In addition, the velocity, energy, and charge of ions are measured far from the irradiated target. As a result, the ion characteristics obtained are affected by collisions and recombination during the post-interaction phase. These processes end at the latest with plasma rarefaction, where ion charges "freeze" at a critical distance L_{cr} from the target. Moreover, ions of different species i form partial currents $j_{i,q}$, which are separated from each other according to their charge state q:

$$j(L,t) = \sum j_{i,q}(L,t), \tag{A1}$$

where L is the distance from the target and t is the TOF.

Revealing the partial currents by decomposition of measured TOF signals and evaluation of Thomson parabolas makes it possible to identify ions with the same mass-to-charge state ratio m/q and also determine their temperature $T_{i,q}$, center-of-mass velocity $u_{\text{CM-}i,q}$, corresponding kinetic energy $E_{\text{CM-}i,q}$, and maximum energy $E_{\max}$.

The signal S of a TOF detector measuring the impacted ions of the same charge in the z direction of the source–detector axis depends on the detector's response to the number of ions and their velocity or energy expressed by the parameter α:

$$S(L,t,\alpha)dS\,dt \propto v_x^{\alpha} f(\vec{v})d\vec{v}, \tag{A2}$$

where $f(\vec{v})$ is the three-dimensional velocity distribution function and

$$\alpha = \begin{cases} 0 & \text{if the response is proportional to the number (density) of incident particles,} \\ 1 & \text{if the response is proportional to the stream (current) of incident particles,} \\ 2 & \text{if the response is proportional to the energy deposited by particles.} \end{cases}$$

Substituting L/t into $f(\vec{v})d\vec{v}$ we get the number of particles hitting the detector's surface area element dS per time interval dt. Since the $d\vec{v} = \left(L/t^4\right)ds\,dt$, $f(\vec{v})d\vec{v}$ in Eq. (A2) is proportional to $f(L/t)Lt^{-4}$ and $S(L,t,\alpha) \sim L^{1+\alpha}\,t^{-(4+\alpha)}\,f(L/t)\,dSdt$.[48,49] If the motion of ionized species can be approximately described by the shifted Maxwell–Boltzmann distribution, then the detector signal can be expressed as

$$S(L,t) = \kappa \frac{L^{\alpha+1}}{t^{\alpha+4}} \exp\left[-\frac{m}{2kT}\left(\frac{L}{t} - u_{CM}\right)^2\right], \tag{A3}$$

where κ is a normalizing factor, m is the mass of species constituting the current j, u_{CM} is the velocity of their center-of-mass motion directed to the ion detector, k is the Boltzmann constant, and T is the ion temperature.

Equation (A3) gives the velocity dependence of the magnitude of the ion current through the term $L^{\alpha+1}/t^{\alpha+4} = v^{\alpha+4}/L^3$. It also explains the significant influence of the type of detector expressed by the term v^{α}, as well as the effect of the fastest ions on the detector signal through their velocity as $v^{\alpha+4}$.

The relationship (3) enables us to determine the time t_{peak} at which the detector's signal reaches a maximum:[50]

$$t_{\mathrm{peak}} = \frac{L}{\alpha+4}\sqrt{\frac{m}{2kT}}\left(\sqrt{2(\alpha+4) + \frac{mu_{\mathrm{CM}}^2}{2kT}} - \sqrt{\frac{mu_{\mathrm{CM}}^2}{2kT}}\right). \tag{A4}$$

Equation (A4) reveals that the term $(\alpha+4)^{-1}$ determines the value of t_{peak} as well as the ion energy E_{peak} at the amplitude peak, which is related to T and $E_{\mathrm{CM}} = \frac{1}{2}mu_{\mathrm{CM}}^2$ as follows:

$$E_{\mathrm{peak}} = \frac{1}{2}m\left(\frac{L}{t_{\mathrm{peak}}}\right)^2 = \frac{1}{4}\left(\sqrt{2(\alpha+4)kT + E_{\mathrm{CM}}} + \sqrt{E_{\mathrm{CM}}}\right)^2. \tag{A5}$$

This relationship gives $E_{\mathrm{peak}} \approx E_{\mathrm{CM}}$ for $T \ll E_{\mathrm{CM}}$ and $E_{\mathrm{peak}} = (\frac{1}{2}\alpha + 2)kT$ for $E_{\mathrm{CM}} = 0$. The relationship (A4) also allows us to determine $v_{\mathrm{peak}} = L/t_{\mathrm{peak}}$.

Determination of E_{CM} of ions is important, since the this corresponds to the potential generated by the release of fast electrons from the plasma through which the ions are accelerated. Previous experiments have shown that in many cases the E_{CM} value is greater than the T value. In these cases, it is no longer production of thermal ions that is taking place. E_{CM} and T values can be determined by decomposition of the TOF detector signal using Eqs. (A2) and (A3) or by corresponding analysis of the experimentally observed energy spectra.

Since the ion current $j(L,t)$ is composed of a certain number of partial currents [Eq. (A1)] of all produced ionized species,[51] the response function of a detector can be expressed as

$$S = \frac{L^{\alpha+1}}{t^{\alpha+4}} \sum S_{i,q} \exp\left[-\frac{m_i}{2kT_{i,q}}\left(\frac{L}{t} - u_{\mathrm{CM}-i,q}\right)^2\right], \tag{A7}$$

where i denotes the ionized species with mass m_i and charge state q, which form a partial current $j_{i,q}$, $S_{i,q}$ is the corresponding response of the detector, $u_{\mathrm{CM}\text{-}i,q}$ is their center-of-mass velocity directed to the ion collector, k is the Boltzmann constant, and $T_{i,q}$ is the corresponding temperature. Decomposition of the TOF detector signal using Eq. (A7) allows us to determine the temperature and center-of-mass velocity of all distinguishable ionized species. Obviously, while decomposition may reveal partial currents, it does not allow us to directly identify the corresponding ionized species. Therefore, for decomposition to be used, it is appropriate to relate temperature to relative atomic mass and to determine the kT/A_r ratio. This, however, does not concern the velocity u_{CM}.

The center-of-mass energy that the ions acquire is due to a potential that is generated by the formation of a double layer caused by the escape of the fastest electrons from the plasma into vacuum.[51] The static electric field E, related to the acceleration potential ϕ, satisfies Poisson's equation based on the local difference in electron density n_e and ion density n_i:

$$\frac{\partial E}{\partial z} = -\frac{\partial^2 \phi}{\partial z^2} = -4\pi e(n_e - \bar{q}n_i), \tag{A8}$$

where e is the electron charge and $\bar{q}$ is the average degree of ionization. We can assume that this potential ϕ_{ef} accelerates ions to energy E_{CM} ($\phi_{ef} = E_{\mathrm{CM}}/e$). The accelerated ions at the front gain maximum energy, while those from the deeper layers of the plasma are accelerated to lower energies owing to shielding of ϕ_{ef}.[52] The measured value of E_{CM} is the result of the whole evolution of the double-layer structure in time and space followed by changes in the electric field. This process ends at the latest with plasma rarefaction, where ion charges "freeze" at a critical distance L_{cr} far from the target, where the observed plasma expansion into the vacuum can be considered collision-free, and therefore ions are detected at $L > L_{\mathrm{cr}}$.[17]

REFERENCES

[1]B. Nagler *et al.*, "Turning solid aluminium transparent by intense soft x-ray photoionization," Nat. Phys. **5**, 693–696 (2009).
[2]A. A. Sorokin, S. V. Bobashev, T. Feigl, K. Tiedtke, H. Wabnitz, and M. Richter, "Photoelectric effect at ultrahigh intensities," Phys. Rev. Lett. **99**, 213002 (2007).
[3]U. Zastrau *et al.*, "XUV spectroscopic characterization of warm dense aluminum plasmas generated by the free-electron-laser FLASH," Laser Part. Beams **30**, 45 (2012).
[4]X. Li, R. Boll, D. Rolles, and A. Rudenko, "Simple model for sequential multiphoton ionization by ultraintense x rays," Phys. Rev. A **104**, 033115 (2021).
[5]H. N. Chapman *et al.*, "Femtosecond diffractive imaging with a soft-x-ray free-electron laser," Nat. Phys. **2**, 839 (2006).
[6]H. N. Chapman *et al.*, "Femtosecond time-delay x-ray holography," Nature **448**, 676 (2007).
[7]C. Bostedt, H. Thomas, M. Hoener *et al.*, "Multistep ionization of argon clusters in intense femtosecond extreme ultraviolet pulses," Phys, Rev. Lett. **100**, 133401 (2008).
[8]K. Falk, "Experimental methods for warm dense matter research," High Power Laser Sci. Eng. **6**, e59 (2018).
[9]S. Preuss, A. Demchuk, and M. Stuke, "Sub-picosecond UV laser ablation of metals," Appl. Phys. A **61**, 33–37 (1995).
[10]S. I. Anisimov and B. S. Luk'yanchuk, "Selected problems of laser ablation theory," Phys.-Usp. **45**, 293–324 (2002).
[11]N. Bityurin, B. S. Luk'yanchuk, M. H. Hong, and T. C. Chong, "Models for laser ablation of polymers," Chem. Rev. **103**, 519–552 (2003).
[12]J. Chalupský *et al.*, "Spot size characterization of focused non-Gaussian x-ray laser beams," Opt. Express **18**, 27836 (2010).
[13]J. Chalupsky *et al.*, "Comparing different approaches to characterization of focused x-ray laser beams," Nucl. Instrum. Methods Phys. Res., Sect. A **631**, 130–133 (2011).
[14]R. Sobierajski *et al.*, "Experimental station to study the interaction of intense femtosecond vacuum ultraviolet pulses with matter at TTF1 free electron laser," Rev. Sci. Instrum. **76**, 013909 (2005).
[15]B. Iwan *et al.*, "TOF-OFF: A method for determining focal positions in tightly focused free-electron laser experiments by measurement of ejected ions," High Energy Density Phys. **7**, 336 (2011).
[16]J. Andreasson *et al.*, "Saturated ablation in metal hydrides and acceleration of protons and deuterons to keV energies with a soft-x-ray laser," Phys. Rev. E **83**, 016403 (2011).
[17]A. Lorusso, J. Krása, K. Rohlena, V. Nassisi, F. Belloni, and D. Doria, "Charge losses in expanding plasma created by an XeCl laser," Appl. Phys. Lett. **86**, 081501 (2005).
[18]M. Manfredda, C. Fava, S. Gerusina, R. Gobessi, N. Mahne, L. Raimondi, A. Simoncig, and M. Zangrando, "The evolution of KAOS, a multipurpose active optics system for EUV/soft x-rays," Synchrotron Radiat. News **35**, 29–36 (2022).
[19]A. A. Sorokin *et al.*, "An x-ray gas monitor for free-electron lasers," J. Synchrotron Radiat. **26**, 1092–1100 (2019).
[20]H. P. Winter, H. Eder, and F. Aumayr, "Kinetic electron emission in the near-threshold region studied for different projectile charges," Int. J. Mass Spectrom. **192**, 407–413 (1999).
[21]J. Krasa, M. Pfeifer, M. P. Stöckli, U. Lehnert, and D. Fry, "The effect of the first dynode's geometry on the detection efficiency of a 119EM electron multiplier used as a highly charged ion detector," Nucl. Instrum. Methods Phys. Res., Sect. B **152**, 397–402 (1999).
[22]J. Chalupský, T. Burian, V. Hájková, L. Juha, T. Polcar, J. Gaudin, M. Nagasono, R. Sobierajski, M. Yabashi, and J. Krzywinski, "Fluence scan: An unexplored property of a laser beam," Opt. Express **21**, 26363 (2013).
[23]V. Vozda *et al.*, "Characterization of megahertz x-ray laser beams by multishot desorption imprints in PMMA," Opt. Express **28**, 25664 (2020).
[24]Y. Okano, H. Kishimura, Y. Hironaka, K. G. Nakamura, and K. Kondo, "X-ray and fast ion generation from metal targets by femtosecond laser irradiation," Appl. Surf. Sci. **197–198**, 281–284 (2002).
[25]S. Amoruso, C. Altucci, R. Bruzzese, C. de Lisio, N. Spinelli, R. Velotta, M. Vitiello, and X. Wang, "Study of the plasma plume generated during near IR femtosecond laser irradiation of silicon targets," Appl. Phys. A **79**, 1377–1380 (2004).
[26]P. A. VanRompay, M. Nantel, and P. P. Pronko, "Pulse-contrast effects on energy distributions of C^{1+} to C^{4+} ions for high-intensity 100-fs laser-ablation plasmas," Appl. Surf. Sci. **127–129**, 1023–1028 (1998).
[27]A. Bulgakov, I. Ozerov, and W. Marine, "Silicon clusters produced by femtosecond laser ablation: Non-thermal emission and gas-phase condensation," Appl. Phys. A **79**, 1591–1594 (2004).
[28]J. Krása, P. Parys, L. Velardi, A. Velyhan, L. Ryć, D. Delle Side, and V. Nassisi, "Time-of-flight spectra for mapping of charge density of ions produced by laser," Laser Part. Beams **32**, 15–20 (2014).
[29]T. H. Tan, G. H. McCall, and A. H. Williams, "Determination of laser intensity and hot-electron temperature from fastest ion velocity measurement on laser-produced plasma," Phys. Fluids **27**, 296–301 (1984).
[30]L. M. Wickens, J. E. Allen, and P. T. Rumsby, "Ion emission from laser-produced plasmas with two electron temperatures," Phys. Rev. Lett. **41**, 243–246 (1978).
[31]J. Krása, A. Velyhan, E. Krouský, L. Láska, K. Rohlena, K. Jungwirth, J. Ullschmied, A. Lorusso, L. Velardi, V. Nassisi, A. Czarnecka, L. Ryć, P. Parys, and J. Wołowski, "Emission characteristics and stability of laser ion sources," Vacuum **85**, 617–621 (2010).
[32]D. Forslund, Inertial Fusion Program: Progress Report LA-7587-PR, Los Alamos Scientific Laboratory, 1980, pp. 93–96.
[33]J. Krása, A. Lorusso, V. Nassisi, L. Velardi, and A. Velyhan, "Revealing of hydrodynamic and electrostatic factors in the center-of-mass velocity of an expanding plasma generated by pulsed laser ablation," Laser Part. Beams **29**, 113–119 (2011).
[34]J. Krása, K. Jungwirth, E. Krouský, L. Láska, K. Rohlena, M. Pfeifer, J. Ullschmied, and A. Velyhan, "Temperature and centre-of-mass energy of ions emitted by laser-produced polyethylene plasma," Plasma Phys. Controlled Fusion **49**, 1649–1659 (2007).
[35]M. Harbst, T. N. Hansen, C. Caleman, W. K. Fullagar, P. Jönsson, P. Sondhauss, O. Synnergren, and J. Larsson, "Studies of resolidification of non-thermally molten InSb using time-resolved x-ray diffraction," Appl. Phys. A **81**, 893–900 (2005).
[36]B. L. Henke, E. M. Gullikson, and J. C. Davis, "X-ray interactions: Photoabsorption, scattering, transmission, and reflection at $E = 50–30\,000$ eV, $Z = 1–92$," At. Data Nucl. Data Tables **54**, 181 (1993), https://henke.lbl.gov/optical_constants/atten2.html.
[37]B. I. Cho *et al.*, "Observation of reverse saturable absorption of an x-ray laser," Phys. Rev. Lett. **119**, 075002 (2017).
[38]M. L. M. Rocco, F. C. Pontes, G. S. Faraudo, and G. G. B. de Souza, "Ionic desorption from PMMA irradiated with multi-bunch synchrotron radiation in the 21.21–300 eV photon energy range," Polym. Degrad. Stab. **84**, 327–330 (2004).
[39]T. E. Haynes, W. K. Chu, T. L. Aselage, and S. T. Picraux, "Initial decomposition of GaAs during rapid thermal annealing," Appl. Phys. Lett. **49**, 666–668 (1986).
[40]W. G. Roeterdink, L. B. F. Juurlink, O. P. H. Vaughan, J. Dura Diez, M. Bonn, and A. W. Kleyn, "Coulomb explosion in femtosecond laser ablation of Si(111)," Appl. Phys. Lett. **82**, 4190–4192 (2003).
[41]N. M. Bulgakova, R. Stoian, A. Rosenfeld, I. V. Hertel, W. Marine, and E. E. B. Campbell, "A general continuum approach to describe fast electronic transport in pulsed laser irradiated materials: The problem of Coulomb explosion," Appl. Phys. A **81**, 345–356 (2005).
[42]R. Stoian, D. Ashkenasi, A. Rosenfeld, and E. E. B. Campbell, "Coulomb explosion in ultrashort pulsed laser ablation of Al_2O_3," Phys. Rev. B **62**, 13167 (2000).
[43]R. Stoian, A. Rosenfeld, I. V. Hertel, N. M. Bulgakova, and E. E. B. Campbell, "Comment on 'Coulomb explosion in femtosecond laser ablation of Si(111)' [Appl. Phys. Lett. 82, 4190 (2003)]," Appl. Phys. Lett. **85**, 694–695 (2004).
[44]W. G. Roeterdink, M. Bonn, and A. W. Kleyn, "Response to "Comment on 'Coulomb explosion in femtosecond laser ablation of Si(111)'" [Appl. Phys. Lett. 85, 694 (2004)]," Appl. Phys. Lett. **85**, 696 (2004).
[45]M. Borghesi, "Laser-driven ion acceleration: State of the art and emerging mechanisms," Nucl. Instrum. Methods Phys. Res., Sect. A **740**, 6–9 (2014).

[46]S. C. Wilks, W. L. Kruer, M. Tabak, and A. B. Langdon, "Absorption of ultra-intense laser pulses," Phys. Rev. Lett. **69**, 1383 (1992).
[47]Z. Chen, C. B. Curry, R. Zhang, F. Treffert, N. Stojanovic, S. Toleikis, R. Pan, M. Gauthier, E. Zapolnova, L. E. Seipp, A. Weinmann, M. Z. Mo, J. B. Kim, B. B. L. Witte, S. Bajt, S. Usenko, R. Soufli, T. Pardini, S. Hau-Riege, C. Burcklen, J. Schein, R. Redmer, Y. Y. Tsui, B. K. Ofori-Okai, and S. H. Glenzer, "Ultrafast multi-cycle terahertz measurements of the electrical conductivity in strongly excited solids," Nat. Commun. **12**, 1638 (2021).
[48]R. Kelly and R. W. Dreyfus, "On the effect of Knudsen-layer formation on studies of vaporization, sputtering, and desorption," Surf. Sci. **198**, 263–276 (1988).
[49]A. Miotello and R. Kelly, "On the origin of the different velocity peaks of particles sputtered from surfaces by laser pulses or charged-particle beams," Appl. Surf. Sci. **138–139**, 44–51 (1999).
[50]J. Krasa, "Gaussian energy distribution of fast ions emitted by laser-produced plasmas," Appl. Surf. Sci. **272**, 46–49 (2013).
[51]S. Eliezer and H. Hora, "Double layers in laser-produced plasmas," Phys. Rep. **172**, 339–407 (1989).
[52]J. Krása, A. Velyhan, K. Jungwirth, E. Krouský, L. Láska, K. Rohlena, M. Pfeifer, and J. Ullschmied, "Repetitive outbursts of fast carbon and fluorine ions from sub-nanosecond laser-produced plasma," Laser Part. Beams **27**, 171–178 (2009).